RSC Advances

PAPER

View Article Online
View Journal | View Issue

Check for updates

Cite this: *RSC Adv.*, 2017, 7, 34522

Catalytic effect of $MnFe_2O_4$ on dehydrogenation kinetics of $NaAlH_4$–MgH_2

Yihui Huang,[a] Ping Li,*[a] Qi Wan,[b] Zhiwei Liu,[a] Wan Zhao,[a] Jun Zhang,[a] Zhili Pan,[a] Li Xu[c] and Xuanhui Qu[a]

Received 24th May 2017
Accepted 4th July 2017

DOI: 10.1039/c7ra05845d

rsc.li/rsc-advances

The hydrogen desorption properties and decomposition processes of $MnFe_2O_4$-doped $NaAlH_4$–MgH_2 composites are investigated. The onset temperatures of three dehydrogenation steps of $MnFe_2O_4$-doped $NaAlH_4$–MgH_2 composites are 92, 116 and 115 °C lower than those of as-milled $NaAlH_4$–MgH_2. Furthermore, $NaAlH_4$–MgH_2 + 3 mol% $MnFe_2O_4$ displays good cycling stability at 300 °C and only a slight capacity loss after four cycles. The apparent activation energies estimated from the Kissinger analysis for $NaAlH_4$- and MgH_2-relevant decomposition are found to be 51.29 and 105.34 kJ mol^{-1}, respectively. XRD and XPS results show that $NaFeO_2$, Mg_2MnO_4 and the amorphous Mn/MnO_x species as well as iron oxides contribute to enhancing the dehydrogenation performance of $NaAlH_4$–MgH_2.

1. Introduction

Hydrogen has attracted global attention as an alternative energy carrier with the aim of reducing society's reliance on fossil fuels.[1] Large gravimetric and volumetric capacities are important for on-board hydrogen storage systems of hydrogen-powered fuel cell vehicles.[2] Therefore, the efficient storage of hydrogen is a key technical issue that requires improvement before its potential can be realized for mobile applications.

It is widely recognized that a major scientific and technological barrier to the commercialization and market acceptance of hydrogen as an energy carrier is the lack of a cheap, safe, and easily produced hydrogen storage material with suitable hydrogen generation kinetics.[3] To date, significant efforts have been directed toward the development of a solid-state hydrogen storage system based on coordination hydrides and related materials, which have been considered as promising storage media owing to their high hydrogen contents and the reversibility of hydrogen uptake.[4,5]

Mg-based material has a high hydrogen storage capacity and good reversibility, and therefore it is an ideal option for hydrogen storage due to its abundant resources and cheap cost. The theoretical hydrogen storage density of a pure MgH_2 system is 7.6 wt%.[6] Nevertheless, the high decomposition temperature (>400 °C) and slow desorption/absorption kinetics have hindered the utilization of MgH_2 in practical onboard applications. To resolve the deficiencies of MgH_2 in terms of hydrogen storage, the hydrogen absorption and desorption properties were improved by many methods, such as nano-crystallization,[7,8] catalyst doping[4,9,10] and reactive hydride composites (RHC).[11,12] Among them, the RHC method was proposed to modify the reaction process by adding a reactive additive.[13] An attractive hydride composite of $NaAlH_4$–MgH_2 has been developed to improve the performance of MgH_2 due to the low hydrogen desorption temperature and excellent cyclability of $NaAlH_4$.[14] It has been proven that an $NaAlH_4$–MgH_2 composite system enhanced dehydrogenation performance compared with ball-milled pure $NaAlH_4$ and MgH_2 alone.[15,16] However, the sluggish kinetics in the $NaAlH_4$–MgH_2 system are another problem that needs to be solved. Additives, such as TiH_2,[17] TiF_3,[18] and Nb_2O_5,[19] are effective in reducing the operating temperature and speeding up the reaction rate for hydrogen storage in $NaAlH_4$–MgH_2. In addition, oxides have been commonly reported to be an effective method of improving the hydrogen storage behaviors of ball-milled pure MgH_2 and $NaAlH_4$ alone.[10,20] More interestingly, further enhanced dehydrogenation kinetics of MgH_2 and $NaAlH_4$ have been achieved by using ferrite oxides.[10,14,20–22] It is speculated that the intermediate compounds formed *in situ* play a vital role in the hydrogen desorption process. Therefore, it is reasonable to assume that ferrite oxide would show great potential as a catalyst to promote the hydrogen storage performances of the $NaAlH_4$–MgH_2 system.

Based on the above discussions, in this work, $MnFe_2O_4$ nanoparticles prepared by an auto-combustion process are used as a catalyst to study the effect on the hydrogen storage performance of $NaAlH_4$–MgH_2 by high-energy ball milling. The catalytic effect on the hydrogen storage properties of $NaAlH_4$–MgH_2 composite is revealed by means of transmission electron microscopy (TEM) investigation.

---

[a] *Institute for Advanced Materials and Technology, University of Science and Technology Beijing, Beijing 100083, China. E-mail: ustbliping@126.com; Fax: +86 10 62334311; Tel: +86 10 62333981*

[b] *Chengdu Institute of Organic Chemistry Chinese Academy of Sciences, Chengdu 610041, China*

[c] *State Key Laboratory of Advanced Transmission Technology, Global Energy Interconnection Research Institute, Beijing 102209, China*

2. Experimental

All reagents and solvent were commercially available and used in the as-received state without further purification. The starting materials used in this study of $Fe(NO_3)_3 \cdot 9H_2O$ (≥95% purity) and $Mn(NO_3)_2$ (≥99% purity) were purchased from Acros Organics. The $MnFe_2O_4$ catalyst was prepared by the nitrate–citrate auto-combustion method, where $Fe(NO_3)_3 \cdot 9H_2O$ and $Mn(NO_3)_2$ were dissolved in deionized water and mixed uniformly before adding the chelating agent citric acid. The pH value of the solution was adjusted to 7 by adding $NH_3 \cdot H_2O$. Then, the solution was stirred by magnetic stirrer at 60 °C to form a sol–gel, which was dried at 120 °C in a vacuum drying chamber. $MnFe_2O_4$ nanoparticles were obtained after the dry gel ignited in air and a self-propagation reaction (exothermic) followed completely. $NaAlH_4$ (≥95% purity) was bought from Alfa Aesar, and MgH_2 (≥99.5% purity) was obtained from Sigma Aldrich. The $NaAlH_4$–MgH_2 composite was prepared by ball milling, a 1 : 1 molar ratio of $NaAlH_4$ and MgH_2 was added to 3 mol% of $MnFe_2O_4$ for 1 h under a high-purity argon atmosphere using a QM-3B high-energy mill (Nanjing Nan Da Instrument Plant, China) at a rotation rate of 1200 rpm. A quantity of 3 g of each mixture was loaded into a stainless steel vessel with a ball-to-powder weight ratio of 20 : 1. The stainless steel balls had diameters of 4 and 8 mm (mass ratio of ball = 1 : 1). To avoid excess heating of the stainless steel vessel, there were 10 min intervals between each 6 min milling process. All samples were transferred and mixed by handling in a glove box (Mikrouna, Super-750) with high-purity argon equipped with a recirculation system (O_2 < 0.1 ppm and H_2O < 0.1 ppm).

The dehydrogenation experiments were measured by using a Sieverts-type pressure-composition-temperature (PCT) apparatus (General Research Institute for Nonferrous Metals, China), which mainly consisted of a reactor and pressure transducer. It was heated to 450 °C at a rate of 5 °C min^{-1} in a static vacuum under a hydrogen pressure of 0.1 MPa to measure the non-isothermal desorption when the 0.3 g sample was loaded. The isothermal desorption properties of the doped samples were manipulated at 300 °C under a vacuum atmosphere.

The structural characteristics of the samples after ball milling and desorption were identified by powder X-ray diffraction (XRD, 40 kV, 300 mA, Cu Kα radiation) with the 2θ angle varying from 20 to 90° at a scanning rate of 5° min^{-1}. X-ray photoelectron spectroscopy (XPS) was performed with a PHI-5300 spectrometer. The morphology and phase constitution of all samples after ball milling and desorption were observed by transmission electron microscopy (TEM, Tecnai G2 F30 S-TWIN, FEI, USA) and energy dispersive X-ray spectrometry (EDX, Tecnai G2 T20, FEI, USA). Differential scanning calorimetry (DSC) experiments were conducted in a Netzsch STA 449 F5 under an argon flow rate of 50 ml min^{-1} from 50 to 450 °C with a heating rate of 5–15 °C min^{-1}. Furthermore, the microstructure and morphology of undoped and doped samples after ball milling and dehydrogenation were identified by field-emission scanning electron microscopy (FESEM, Quanta FEG 650).

3. Results and discussion

The nanocrystalline $MnFe_2O_4$ composite was prepared by the auto-combustion process. XRD patterns (Fig. 1(a)) of $MnFe_2O_4$ nanoparticles can be perfectly assigned to the cubic phase of $MnFe_2O_4$ (PDF: 74-2403). The diffraction peaks can be seen at 30.1°, 35.08°, 42.82°, 53.23°, 56.89°, 62.65° and 73.82°, corresponding to the (220), (311), (400), (422), (511), (440) and (533) planes of $MnFe_2O_4$. The average grain size of $MnFe_2O_4$ is 38 nm, calculated by the Scherrer formula based on the characteristic peaks. A typical TEM micrograph (Fig. 1(b)) of $MnFe_2O_4$ particles indicated multidispersed particles with a mean diameter of about 40 nm. The electron diffraction pattern indicated that the modified $MnFe_2O_4$ particles were crystallized. The small particles are one of the vital elements for catalyzed reactions and have a great impact on the decomposition temperature and hydrogen capacity.[14,23,24]

Fig. 2 demonstrates the XRD patterns of the doped samples. In the XRD spectrum of the as-milled $NaAlH_4$–MgH_2 in Fig. 2(a), several $NaAlH_4$ and MgH_2 peaks can be found, indicating that there is no detectable reaction between $NaAlH_4$ and MgH_2 during the ball-milling process. As shown in Fig. 2(b), a new phase, Al, was identified in the $MnFe_2O_4$-doped sample although the $NaAlH_4$ and MgH_2 phases still dominated the XRD pattern. This shows that a significant amount of $NaAlH_4$ is still stable and only a small portion is broken down into Al during the ball-milling process. In addition, the quite broad diffraction peaks compared to the as-milled $NaAlH_4$–MgH_2 suggest poor crystallization or small particle sizes.

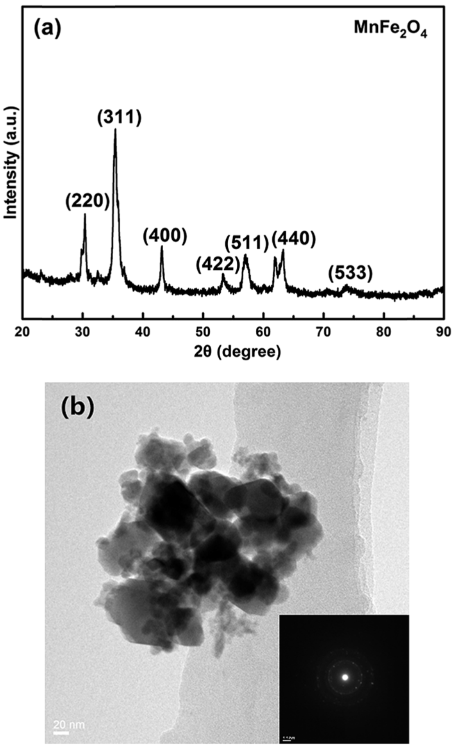

Fig. 1 (a) XRD and (b) TEM patterns of synthesized $MnFe_2O_4$.

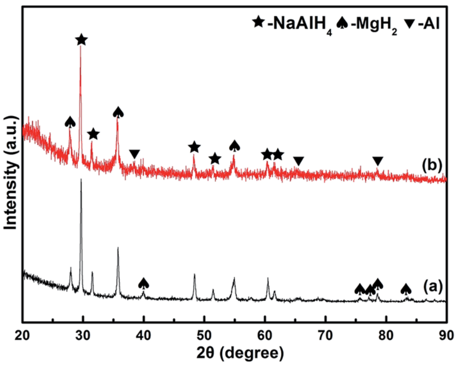

Fig. 2 XRD patterns of: (a) as-milled $NaAlH_4$–MgH_2, (b) as-milled $NaAlH_4$–MgH_2 + 3 mol% $MnFe_2O_4$.

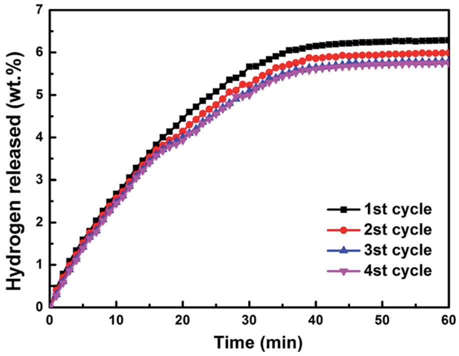

Fig. 4 Cycling dehydrogenation curves of the samples hydrogenated at 300 °C in the initial four cycles.

In order to investigate the effects of manganese ferrite oxide on the desorption temperature among the two hydrides, thermal desorption curves of the doped samples are compared, as shown in Fig. 3. As can be seen in Fig. 3(d), the as-milled $NaAlH_4$–MgH_2 + 3 mol% $MnFe_2O_4$ sample starts to desorb hydrogen at 80, 204 and 308 °C for the three steps respectively. The onset dehydrogenation temperatures of $NaAlH_4$–MgH_2 + 3 mol% $MnFe_2O_4$ are individually reduced by 92, 116 and 115 °C, respectively, compared with those of as-milled $NaAlH_4$–MgH_2 (Fig. 3(a)). This reveals that $MnFe_2O_4$ nanoparticles have a significant effect on the dehydrogenation temperatures of $NaAlH_4$–MgH_2. Meanwhile, the initial temperatures of the three dehydrogenation steps of as-milled $NaAlH_4$ + 3 mol% $MnFe_2O_4$ (Fig. 3(b)) are 126, 183 and 267 °C, respectively, and as-milled MgH_2 + 3 mol% $MnFe_2O_4$ (Fig. 3(c)) starts to decompose at 340 °C. After they are combined together, the onset decomposition temperature of $NaAlH_4$ and MgH_2 in the $MnFe_2O_4$-doped composite is 46 °C, 42 °C lower than that of its unary components ($NaAlH_4$ and MgH_2), which indicates that the dehydrogenation performance of $NaAlH_4$ and MgH_2 is significantly improved by a mutual destabilization. In addition, it eventually liberates 6.75 wt% hydrogen, and 5.5 wt% hydrogen can be obtained below 250 °C. Consequently, through comprehensively considering the dehydrogenation temperature and total hydrogen content, it is reasonable to conclude that $NaAlH_4$–MgH_2 doped with 3 mol% $MnFe_2O_4$ ferrites exhibits optimal dehydrogenation properties.

Considering hydrogen storage reversibility of the nanocrystalline $MnFe_2O_4$-containing $NaAlH_4$–MgH_2, the dehydrogenated samples were isothermally hydrogenated at 300 °C then subjected to re-dehydrogenation under 3 MPa hydrogen pressure as a function of temperature. The dehydrogenation curves of the nanocrystalline $MnFe_2O_4$-containing $NaAlH_4$–MgH_2 in the first four cycles are shown in Fig. 4. The $MnFe_2O_4$-added sample exhibits quite good cyclability, and hydrogen desorption amount remained at 4.30 wt% after four cycles. The corresponding desorption capacity retention was calculated to be nearly 90%, which is distinctly superior to the results reported previously.[17–19] Accordingly, it is believed that the cyclability of $NaAlH_4$–MgH_2 is enhanced by adding $MnFe_2O_4$.

The $NaAlH_4$–MgH_2 composite system is further investigated by DSC, as shown in Fig. 5. One distinct exothermic peak and four distinct endothermic peaks are observed for the as-milled $NaAlH_4$–MgH_2 (Fig. 5(a)) during the heating process. The exothermic peak at 168.5 °C is due to the presence of surface hydroxyl impurities in $NaAlH_4$, as reported in our previous studies.[6,20] The first endothermic peak at 182.1 °C can be attributed to the decomposition of $NaAlH_4$, while the second endothermic peak at 255.9 °C is due to the decomposition of Na_3AlH_6.[14] The last two endothermic peaks at 359.8 and

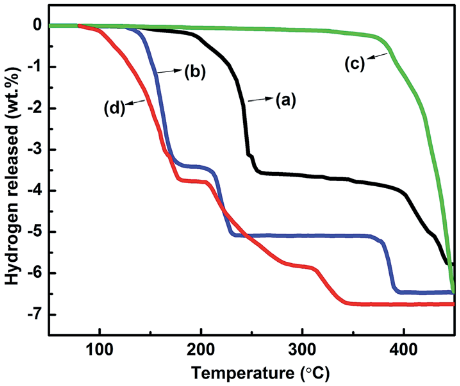

Fig. 3 Thermal dehydrogenation profiles of ball-milled sample: (a) $NaAlH_4$–MgH_2, (b) $NaAlH_4$ + 3 mol% $MnFe_2O_4$, (c) MgH_2 + 3 mol% $MnFe_2O_4$, (d) $NaAlH_4$–MgH_2 + 3 mol% $MnFe_2O_4$.

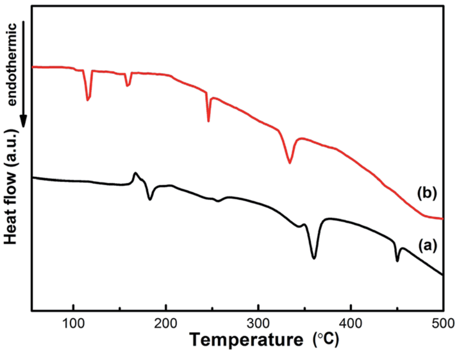

Fig. 5 DSC traces of as-milled sample: (a) $NaAlH_4$–MgH_2, (b) $NaAlH_4$–MgH_2 + 3 mol% $MnFe_2O_4$.

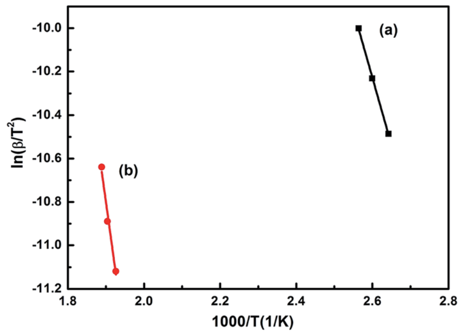

Fig. 6 Kissinger plot of the dehydrogenation for (a) $NaAlH_4$- and (b) MgH_2-relevant decomposition.

450.1 °C correspond to the decomposition of MgH_2 and NaH, respectively.[15,16] It is notable that the endothermic peak of the melting of $NaAlH_4$ disappeared in the DSC profiles of as-milled $NaAlH_4$–MgH_2 + 3 mol% $MnFe_2O_4$ in Fig. 5(b). All four endothermic events in the case of as-milled $NaAlH_4$–MgH_2 + 3 mol% $MnFe_2O_4$ have been shifted to lower temperature, and are, respectively, assigned to the decomposition of $NaAlH_4$-, Na_3AlH_6-, MgH_2- and NaH-relevant at 115.3, 160.5, 246.0 and 334.0 °C.[20,24–26] The results show that $NaAlH_4$ and MgH_2 decomposes without melting with $MnFe_2O_4$ nanoparticles at a much lower temperature. One finds that the onset decomposition temperature in the DSC curves is slightly higher than that in the PCT curves, which may be because the dehydrogenation measurements were run under different conditions in these two cases, as was the case in our previous studies.[20,22]

To further investigate the effect of $MnFe_2O_4$ nanoparticles on the kinetic barrier of commercial $NaAlH_4$–MgH_2, the activation energy of 3 mol% $MnFe_2O_4$ + $NaAlH_4$ is calculated using the Kissinger method.[17] Thus, the activation energy (E_a) can be obtained from the slope on a plot of $\ln(\beta T_p^{-2})$ *versus* $1000/T_p$ from DSC curves with heating rates of 5, 10 and 15 °C min^{-1}. Fig. 6 shows the Kissinger plots of the $NaAlH_4$–MgH_2 doped with 3 mol% $MnFe_2O_4$. The apparent E_a values estimated from the Kissinger analysis for $NaAlH_4$- and MgH_2-relevant decomposition were found to be 51.29 and 105.34 kJ mol^{-1}, respectively, which is lower compared to other catalysts.[14,17,19] The result indicates that $MnFe_2O_4$ obviously decreases the kinetic barrier for dehydrogenation of $NaAlH_4$–MgH_2, providing a quantitative basis for improving the kinetics performance of dehydrogenation.

To understand the chemical events occurring in the ball milling and thermal desorption processes, the $MnFe_2O_4$-doped and dehydrogenated samples at different temperatures were subjected to XRD measurements, as shown in Fig. 7. It can be seen that there is no detectable reaction between $NaAlH_4$ and MgH_2 at 70 °C and part of the Al phase is derived from the decomposition of $NaAlH_4$ during ball milling. After heating to 120 °C, the new peaks of Na_3AlH_6 appear, while the peak of MgH_2 still exists. The fact that the peak intensities of Al increased and the peak of $NaAlH_4$ weakened indicated that the reaction in eqn (1) has taken place, as shown below:

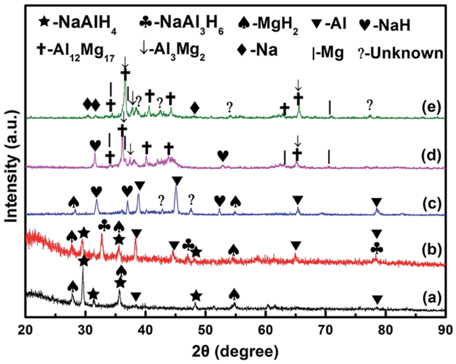

Fig. 7 XRD patterns of as-milled $NaAlH_4$–MgH_2 + 3 mol% $MnFe_2O_4$ dehydrogenated at (a) 70 °C, (b) 120 °C, (c) 200 °C, (d) 300 °C and (e) 350 °C.

$$3NaAlH_4 \rightarrow Na_3AlH_6 + 2Al + 3H_2 \tag{1}$$

When the dehydrogenation temperature was increased to 200 °C, the appearance of NaH indicated that Na_3AlH_6 was partially decomposed, which is consistent with the first two stages of the DSC curves. After further heating to 300 °C, the peaks of $Mg_{17}Al_{12}$, Mg_2Al_3 and Mg were observed, and the peaks of MgH_2 and Al phases disappeared. Typically, this step is associated with the formation of intermediate hydrides.[12,25] So, the main reaction in eqn (2)–(4) involved in this step may take place:

$$12Al + 17MgH_2 \rightarrow Mg_{17}Al_{12} + 17H_2 \tag{2}$$

$$2Al + 3MgH_2 \rightarrow Mg_3Al_2 + 3H_2 \tag{3}$$

$$MgH_2 \rightarrow Mg + 3H_2 \tag{4}$$

When the dehydrogenation temperature was increased to 350 °C, the intensity of $Mg_{17}Al_{12}$ and Mg_3Al_2 phases became stronger and the peaks of NaH phases disappeared, indicating that the system was fully dehydrogenated. These results also confirmed that the hydrogen released in the third stage was from the MgH_2-relevant decomposition through the reaction in eqn (2)–(4), while the decomposition of NaH in eqn (5) is related to the last stage, as illustrated below:

$$NaH \rightarrow Na + 0.5H_2 \tag{5}$$

According to the above results, $Mg_{17}Al_{12}$ and Mg_3Al_2 phases are observed during dehydrogenation, which is in accord with literature reports.[15–19,24] It is expected that the formation of the $Mg_{17}Al_{12}$ and Mg_3Al_2 phases during dehydrogenation enhances thermodynamic properties of $NaAlH_4$–MgH_2. There are some unknown diffraction peaks after dehydrogenation at 200 °C, indicating the existence of a crystallized phase. However, there are no diffraction peaks of Mn- or Fe-containing species. This is believed to be mainly because the Mn or Mn-containing phases are unknown or in amorphous state. As discussed in our previous studies,[10,20] the formation of Fe–O and amorphous Mn/

MnO_x species plays a vital role in enhancing dehydrogenation properties of $NaAlH_4$ and MgH_2. XPS spectroscopy of $MnFe_2O_4$-doped sample was carried out to further investigate the nature of the Mn and Fe species after ball-milling and dehydrogenation.

Initial XPS measurements were carried out on the Mn 2p and Fe 2p peaks of $MnFe_2O_4$ in Fig. 8(a and b). As can be seen, the Fe $2p_{3/2}$ spectrum was registered at 710.8 eV and the Fe $2p_{1/2}$ spectrum was registered at 724.8 eV, which indicated fully oxidized iron on the surface.[27] In addition, the Fe $2p_{3/2}$ peak is stronger than that of Fe $2p_{1/2}$ and its area is greater than that of Fe $2p_{1/2}$ because Fe $2p_{3/2}$ has degeneracy of four states while Fe $2p_{1/2}$ has only two in spin–orbit (j–j).[28] There is a satellite line of the Fe $2p_{3/2}$ peak around 719.1 eV.[29] The XPS peaks of Mn 2p centered at 642.8 and 653.8 eV, respectively, come from either Mn(II) or Mn(VI).[30,31] Therefore, Mn is solely bivalent according to the valence of Fe. By referring to the two-phase diagram, there were no corresponding intermetallic compounds between Fe and Mn because they could not dissolve each other. Furthermore, the satellite line of the Fe $2p_{3/2}$ peak disappeared after ball-milling in Fig. 8(c), and the intensities of the peaks were weaker than the Fe 2p peaks of $MnFe_2O_4$, especially the Fe $2p_{3/2}$ spectrum at 712.5 eV. After dehydrogenation at 350 °C, the signal at 711.3 eV is assigned to $NaFeO_2$ in Fig. 8(e) and others at 724.3 and 732.7 eV are attributed to iron oxides.[32] For Mn 2p, the peaks in Fig. 8(d) appearing at 641.3 and 653.8 eV, which correspond to MnO_x/Mn phase indicated that Mn(II) or Mn(VI) had transformed into amorphous oxides after ball-milling. However, after heating to 350 °C, the status of manganese was not affected by the desorption reaction, in Fig. 8(f), but a slight peak appeared at 646.8 eV. Li reported that Mg_2MnO_4 nanoparticles was observed after milling or upon desorption reactions of Mn-based MgH_2 doped systems.[10] It is reasonable to be assume that a small amount of Mg_2MnO_4 can also be formed in

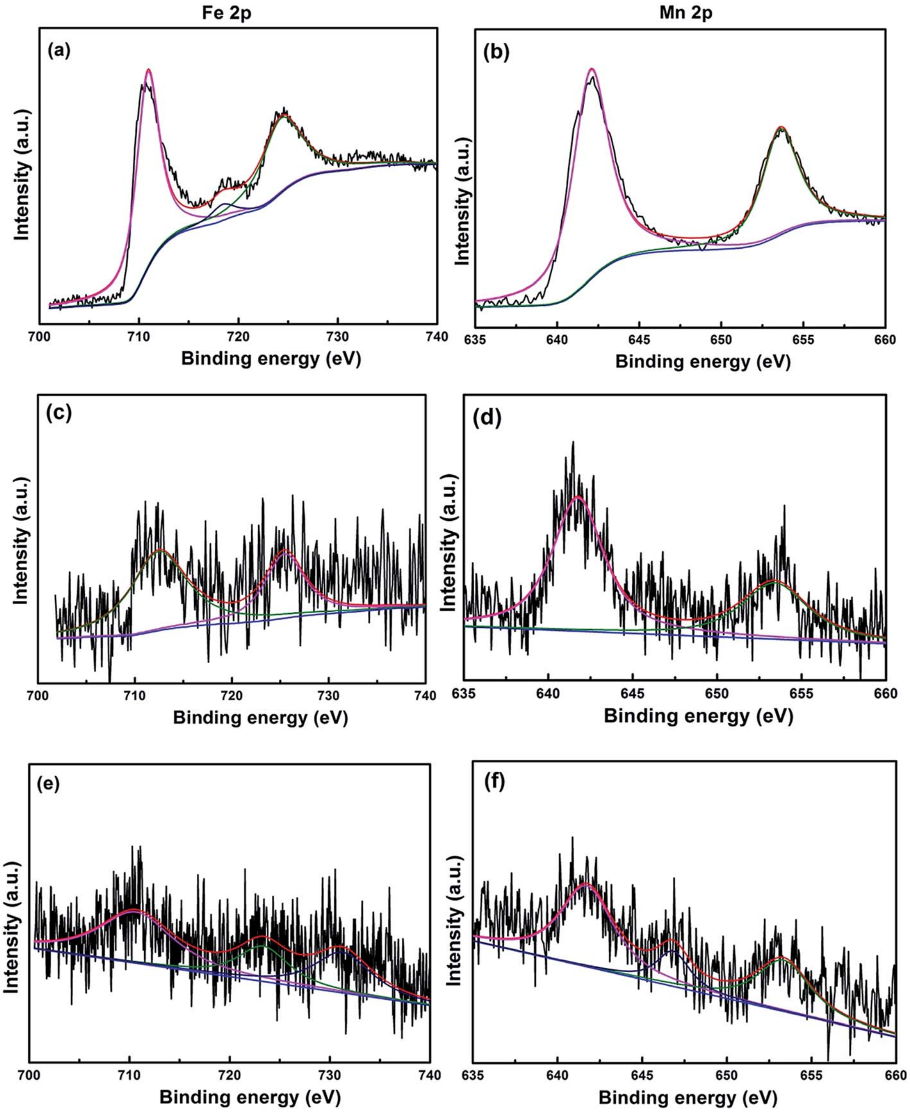

Fig. 8 XPS spectra: (a) Fe 2p and (b) Mn 2p of $MnFe_2O_4$; (c) Fe 2p and (d) Mn 2p of $MnFe_2O_4$-doped $NaAlH_4$–MgH_2; (e) Fe 2p and (f) Mn 2p of $MnFe_2O_4$-doped $NaAlH_4$–MgH_2 dehydrogenated at 350 °C.

Mn-based $NaAlH_4$–MgH_2 doped systems. Therefore, the unknown phases may be $NaFeO_2$ and Mg_2MnO_4, the amorphous phases may be Mn/MnO_x species as well as iron oxides, which also worked together in improving dehydrogenation properties of $NaAlH_4$–MgH_2.[10,14,20]

The dehydrogenation/hydrogenation properties are closely related with particle sizes and surface defects. For a better understanding of the potential destabilization mechanism of $NaAlH_4$–MgH_2 doped with $MnFe_2O_4$, the FESEM images of the sample are shown in Fig. 9. The images show that the size of $NaAlH_4$–MgH_2 (Fig. 9(a)) is different after milling and the particle diameters is distributed in the range of 3–5 μm. However, the particles are close together, which is not conducive to hydrogen desorption kinetics. Compared to the as-milled $NaAlH_4$–MgH_2, the particle size of as-milled $NaAlH_4$–MgH_2 with 3 mol% $MnFe_2O_4$ nanoparticles (Fig. 9(c)) became smaller (about 100–500 nm) and uniform. Although there are some clusters in the $MnFe_2O_4$-doped sample, the grain boundaries between the particles can be clearly seen, which proves that the introduction of $MnFe_2O_4$ has brought about a decrease in the size of the particles. The refined particle size renders much shorter diffusion paths for hydrogen in the dehydrogenation/hydrogenation process.[20,22] This ability is one of the reasons why adding $MnFe_2O_4$ nanoparticles improves the $NaAlH_4$–MgH_2 kinetics, as these nanosized particles may serve as nucleation sites and create more grain boundaries at the surface of the $NaAlH_4$–MgH_2 matrix. As shown in Fig. 9(b), the particle size of $NaAlH_4$–MgH_2 after dehydrogenation has no obvious change, but its distribution is more uniform than before desorption. It can also be seen that the particle size of the $MnFe_2O_4$-doped sample after dehydrogenation (Fig. 9(d)) is reduced and has become uniform. Therefore, this may be the reason for a partial reversibility after the $MnFe_2O_4$ catalyst is added. It should be noted that the embedded $MnFe_2O_4$ cannot be observed in the $NaAlH_4$–MgH_2 surface owing to its nanoparticle size, which is consistent with the result of TEM images (Fig. 1(b)) of $MnFe_2O_4$.

TEM micrograph observation is performed to analyze the condition of $MnFe_2O_4$ distributed in the matrix of $NaAlH_4$–MgH_2 at nanometer scale. Fig. 10 shows dark field images, high resolution transmission electron microscopy and energy dispersive X-ray detector analyses of the as-milled $NaAlH_4$–MgH_2 + 3 mol% $MnFe_2O_4$ sample. In Fig. 10(a), some black particles are homogenously distributed among the gray matrix. To determine what these particles are, corresponding EDX measurements of the black area A and the gray area B are conducted, as shown in Fig. 10(c) and (d), respectively. For the black regions, Mn, Fe, O, Na, Mg and Al are identified by the EDS analysis, where Mg, Na and Al are derived from the basis material. However, Mn and Fe elements are detected in the gray areas, where their intensity is much weaker than in the black area. Thus, it could be deduced that the black nanoparticles are $NaAlH_4$–MgH_2 and the gray nanoparticles correspond to $MnFe_2O_4$-doped $NaAlH_4$–MgH_2 matrix. The values of interlamellar spacing in Fig. 10(b) are 2.51 and 1.86 nm, corresponding to $NaAlH_4$ and MgH_2, respectively. In addition, the boundaries appear as a large number of defects, which will be the paths for hydrogen diffusion.[21,22]

The electron micrograph of dehydrogenated $MnFe_2O_4$-doped sample is shown in Fig. 11(a), which indicates that the catalyst

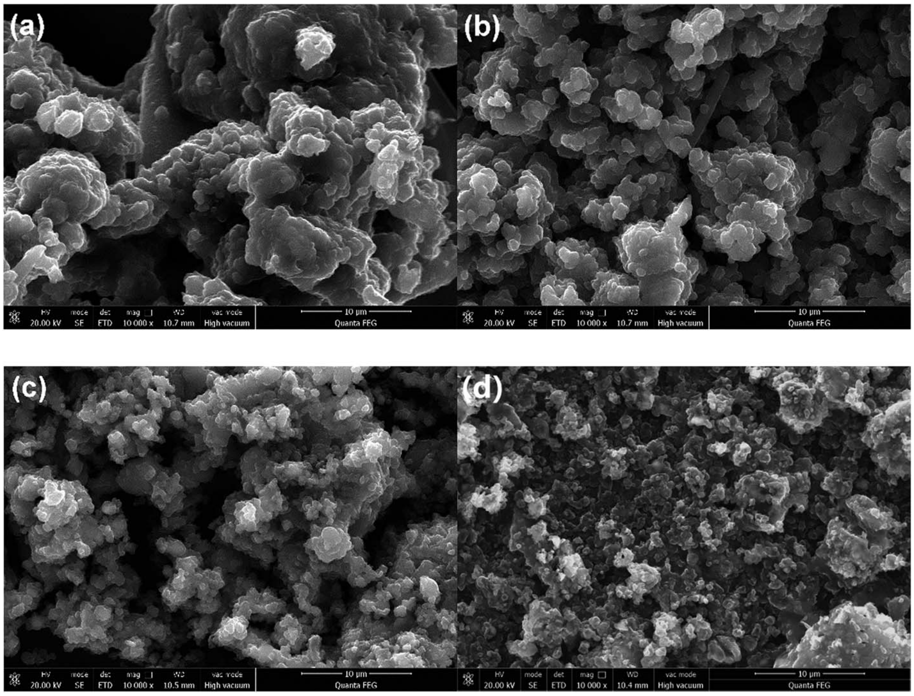

Fig. 9 FESEM image of: (a) as-milled $NaAlH_4$–MgH_2, (b) as-milled $NaAlH_4$–MgH_2 after desorption in 300 °C, (c) as-milled $NaAlH_4$–MgH_2 + 3 mol% $MnFe_2O_4$, (d) as-milled $NaAlH_4$–MgH_2 + 3 mol% $MnFe_2O_4$ after desorption in 300 °C.

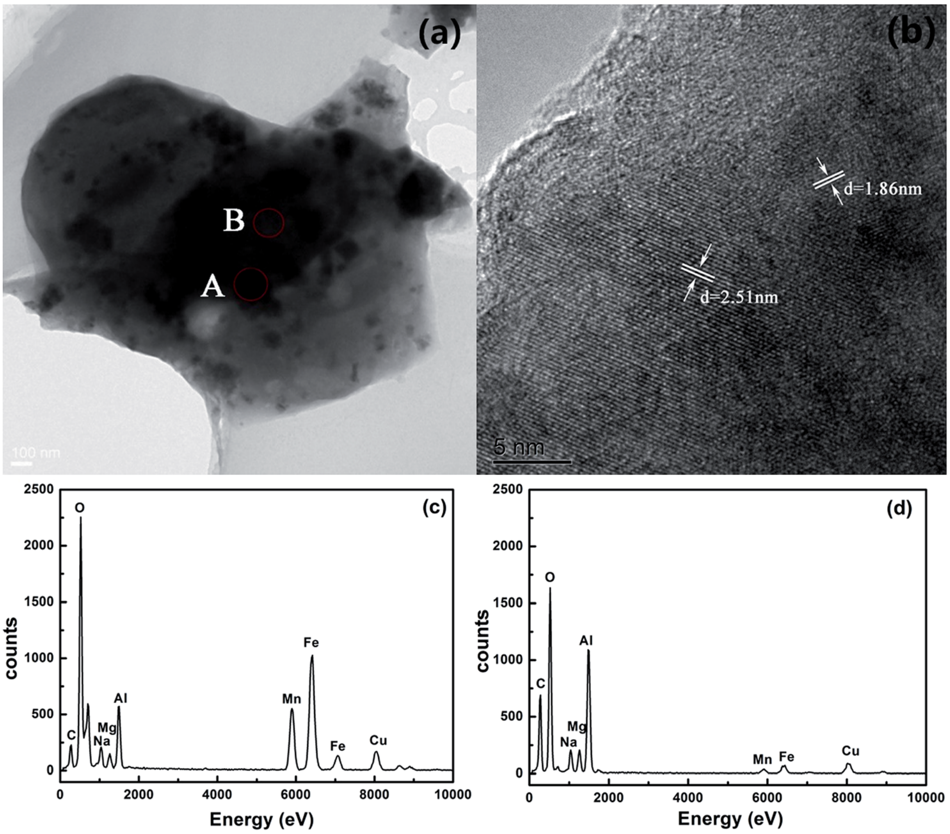

Fig. 10 (a) TEM and (b) HRTEM micrographs; EDX: (c) A region and (d) B region are results of as-milled $NaAlH_4$–MgH_2 + 3 mol% $MnFe_2O_4$.

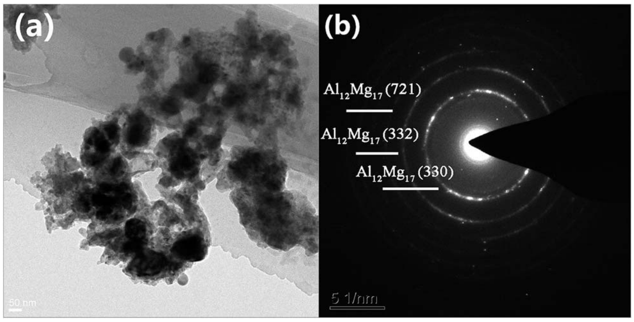

Fig. 11 (a) TEM micrographs and (b) SAED pattern of as-milled $NaAlH_4$–MgH_2 + 3 mol% $MnFe_2O_4$ after dehydrogenation at 350 °C.

is still uniformly distributed in the $NaAlH_4$–MgH_2 matrix after dehydrogenation. To further investigate the microstructure of $MnFe_2O_4$-doped sample, selected area electronic diffraction results are shown in Fig. 11(b). The diffraction rings could be well indexed with crystal planes of $Al_{12}Mg_{17}$ (330), $Al_{12}Mg_{17}$ (332) and $Al_{12}Mg_{17}$ (721), which is in good agreement with the XRD analysis.

4. Conclusion

The onset temperatures of the dehydrogenation steps of $MnFe_2O_4$-doped $NaAlH_4$–MgH_2 composites are 92, 116 and 115 °C lower than those of as-milled $NaAlH_4$–MgH_2, respectively. Furthermore, $NaAlH_4$–MgH_2 + 3 mol% $MnFe_2O_4$ displays good cycle stability at 300 °C and only a slight capacity loss after four cycles. The apparent activation energies estimated from the Kissinger analysis for $NaAlH_4$- and MgH_2-relevant decomposition are found to be 51.29 and 105.34 kJ mol^{-1}, respectively. XRD and XPS results show that $NaFeO_2$, Mg_2MnO_4 and the amorphous Mn/MnO_x species as well as iron oxides contribute to enhancing dehydrogenation performance of $NaAlH_4$–MgH_2.

Acknowledgements

This study was financially supported by the National Natural Science Foundation of China (NSFC, Grant No. 51471054) and Beijing Natural Science Foundation (BNSF, 2152019). The authors would like to thank Liu ran from shiyanjia lab for the support of XPS analysis.

References

1 U. Eberle, M. Felderhoff and F. Schüth, *Angew. Chem., Int. Ed.*, 2009, **48**, 6608–6630.
2 L. Schlapbach and A. Züttel, *Nature*, 2001, **414**, 353–358.
3 N. Juahir, N. S. Mustafa, A. Sinin and M. Ismail, *RSC Adv.*, 2015, **5**, 60983–60989.

4 J. Lu, Y. J. Choi, Z. Z. Fang, H. Y. Sohn and E. Rönnebro, *J. Am. Chem. Soc.*, 2009, **131**, 15843–15852.

5 Y. P. Pang, Y. F. Liu, M. X. Gao, L. Z. Ouyang, J. W. Liu, H. Wang, M. Zhu and H. G. Pan, *Nat. Commun.*, 2014, **5**, 3519.

6 X. Zhang, Y. F. Liu, K. Wang, M. X. Gao and H. G. Pan, *Nano Res.*, 2015, **8**, 533–545.

7 A. S. Gangrade, A. A. Varma, N. K. Gor, S. Shriniwasana and S. S. V. Tatiparti, *Phys. Chem. Chem. Phys.*, 2017, **19**, 6677–6687.

8 B. Paik, I. P. Jones, A. Walton, V. Mann, D. Book and I. R. Harris, *J. Alloys Compd.*, 2010, **492**, 515–520.

9 G. Sun, Y. Li, X. Zhao, J. Wu, L. Wang and Y. Mi, *RSC Adv.*, 2016, **6**, 23110–23116.

10 P. Li, Q. Wan, Z. L. Li, F. Q. Zhai, Y. L. Li, L. Q. Cui, X. H. Qu and A. A. Volinsky, *J. Power Sources*, 2013, **239**, 201–206.

11 H. Liu, X. Wang, Y. Liu, Z. Dong, H. Ge, S. Li and M. Yan, *J. Phys. Chem. C*, 2014, **118**, 37–45.

12 F. Cova, F. C. Gennari and P. A. Larochette, *RSC Adv.*, 2015, **5**, 90014–90021.

13 J. J. Vajo and G. L. Olson, *Scr. Mater.*, 2007, **56**, 829–834.

14 Y. H. Huang, P. Li, Q. Wan, J. Zhang, Y. Li, R. W. Li, X. P. Dong and X. H. Qu, *J. Alloys Compd.*, 2017, **709**, 850–856.

15 M. Ismail, Y. Zhao, X. B. Yu, J. F. Mao and S. X. Dou, *Int. J. Hydrogen Energy*, 2011, **36**, 9045–9050.

16 A. Bhatnagara, S. K. Pandeya, V. Dixita, V. Shuklaa, R. R. Shahib, M. A. Shaza and O. N. Srivastavaa, *Int. J. Hydrogen Energy*, 2014, **39**, 14240–14246.

17 H. H. Cheng, Y. Chen, W. P. Sun, H. R. Lou, Y. Q. Liu, Q. Qi, J. M. Zhang, J. J. Liu, K. Yan, H. M. Jin, Y. Zhang and S. Y. Yang, *J. Alloys Compd.*, 2017, **698**, 1002–1008.

18 M. Ismail, Y. Zhao, X. B. Yu and S. X. Dou, *Int. J. Hydrogen Energy*, 2012, **37**, 8395–8401.

19 R. U. Din, X. H. Qu, P. Li, L. Zhang, M. Ahmad, M. Z. Iqbal, M. Y. Rafique and M. H. Farooq, *RSC Adv.*, 2012, **2**, 4891–4903.

20 Q. Wan, P. Li, Z. L. Li, K. F. Zhao, Z. W. Liu, L. Wang, F. Q. Zhai, X. H. Qu and A. A. Volinsky, *J. Power Sources*, 2014, **248**, 388–395.

21 F. Q. Zhai, P. Li, A. Z. Sun, S. Wu, Q. Wan, W. N. Zhang, Y. L. Li, L. Q. Cui and X. H. Qu, *J. Phys. Chem. C*, 2012, **116**, 11939–11945.

22 J. Zhang, P. Li, Q. Wan, F. Q. Zhai, A. A. Volinsky and X. H. Qu, *RSC Adv.*, 2015, **5**, 81212–81219.

23 R. J. Xiong, G. Sang, G. H. Zhang, X. Y. Yan, P. L. Li, Y. Yao, D. Luo, C. Chen and T. Tang, *Int. J. Hydrogen Energy*, 2017, **42**, 6088–6095.

24 J. K. Bendyna, S. Dyjak and P. H. L. Notten, *Int. J. Hydrogen Energy*, 2015, **40**, 4200–4206.

25 M. Ismail and N. S. Mustafa, *Int. J. Hydrogen Energy*, 2016, **41**, 18107–18113.

26 Y. J. Kwak, S. H. Lee, B. S. Lee, H. R. Park and M. Y. Song, *J. Nanosci. Nanotechnol.*, 2015, **15**, 8763–8772.

27 T. J. Daou, G. Pourroy, S. Bégin-Colin, J. M. Grenèche, C. Ulhaq-Bouillet, P. Legaré, P. Bernhardt, C. Leuvrey and G. Rogez, *Chem. Mater.*, 2006, **18**, 4399–4404.

28 T. Yamashita and P. Hayes, *Appl. Surf. Sci.*, 2008, **254**, 2441–2449.

29 J. Li, Y. Jiao and C. C. Wan, *Front. Agr. Sci. Eng.*, 2017, **4**, 116–120.

30 K. Yan, Y. Lu and W. Jin, *ACS Sustainable Chem. Eng.*, 2016, **4**, 5398–5403.

31 J. Hu, M. C. L. Irene and G. H. Chen, *Langmuir*, 2005, **21**, 11173–11179.

32 M. Descostes, F. Mercier, N. Thromat, C. Beaucaire and M. Gautier-Soyer, *Appl. Surf. Sci.*, 2000, **165**, 288–302.